aerospace

MDPI

Article

Design and Experimental Study of a Turbojet VTOL Aircraft with One-Dimensional Thrust Vectoring Nozzles

Benshan Liu, Yongsheng Gao, Liang Gao *, Junming Zhang, Yanhe Zhu, Xizhe Zang and Jie Zhao *

State Key Laboratory of Robotics and System, Harbin Institute of Technology, Harbin 150001, China
* Correspondence: gaoliang@hit.edu.cn (L.G.); jzhao@hit.edu.cn (J.Z.)

Abstract: Turbojet engines have a slow response and require mechanical assistance to perform vertical take-offs and landings. In this paper, we propose a vertical take-off and landing (VTOL) aircraft that contains one-dimensional thrust vectoring nozzle modules to solve the problem of dependence on the response of the turbojet. The turbojet engine is placed horizontally in the module, the rotational speeds are fixed, and the force along the turbojet axis remains constant as the nozzle rotates from the horizontal to the vertical position. The aircraft is composed of four modules, whose position and attitude control are realized by using the thrust difference caused by the different angles of the four vector nozzles. The modules no longer rely on the response speed of the turbojet engine, and controlling the angles of four nozzles makes it easier to operate the aircraft. The horizontal placement of the turbojet can reduce the thickness of the aircraft fuselage and decrease air resistance. The process of moving the nozzle from a horizontal to a vertical position prevents the engine from blowing directly on the ground and, thus, reduces the ground effect.

Keywords: thrust vectoring nozzle; turbojet aircraft; VTOL

Citation: Liu, B.; Gao, Y.; Gao, L.; Zhang, J.; Zhu, Y.; Zang, X.; Zhao, J. Design and Experimental Study of a Turbojet VTOL Aircraft with One-Dimensional Thrust Vectoring Nozzles. *Aerospace* **2022**, *9*, 678. https://doi.org/10.3390/aerospace9110678

Academic Editor: Peng Wei

Received: 3 October 2022
Accepted: 29 October 2022
Published: 2 November 2022

1. Introduction

In the past, turbojet vertical take-off and landing (VTOL) aircraft were mainly used in the military, and their advantages of a large thrust-to-weight ratio and high fuel efficiency also have broad application prospects in emergency transportation and rescue and other fields. VTOL aircraft have simple requirements for take-off and landing sites, can provide precise hovering and good maneuverability, and are very flexible [1]. They can not only independently complete intelligent inspections [2], but they can also protect agricultural developments [3], support logistics and distribution [4], and complete other tasks. Additionally, VTOLs can provide mobile platforms for cross-domain operations, such as airborne mobile arms operations [5] and Leonardo [6], which have particularly high requirements for load capacity and mobility.

Common VTOL power units include electric propellers and turbojets [7]. The authors of [8] summarized the detailed design of specific drone elements and propulsion components. There are many platforms powered by electric propellers, such as ducted [9], dual-rotor, tri-rotor, quad-rotor, and vector quad-rotor propulsion systems. Their overall characteristics are ease of use, fast response speed, and high stability of the motor. The disadvantage is that the propeller is bulky when there is a certain load, and the battery is located in the fuselage, where it is a fixed structural weight. The energy density of the battery is less than that of fuel oil, and the specific energy of the lithium-ion battery is approximately 120~200 w·h/kg, which is much less than that of fuel oil, i.e., 12 kw·h/kg [10]. In contrast, the advantages of the turbojet VTOL aircraft are the large thrust-to-weight ratio and compact structure. Under the same load conditions, the volume is smaller than that of propeller-type platforms. At present, the turbojet VTOL aircraft that have been applied in the military field mainly include the British Harrier, AV-8A of the US Marine Corps, Jacques-38 and Jacques-141 developed by the former Soviet Union, and F-35B of the US [11].

The mathematical modeling of the Jetcat P200SX micro turbojet engine was reported in the literature [12]. Turbojet aircraft usually use vector thrusting rather than the differential speed of the turbojet engine to achieve vertical take-off and landing, as the speed response process of the turbojet engine is much slower than that of motors. There are three ways to achieve thrust vectoring: to tilt the engine, to use the lift engine and main engine at the same time, and to deflect the nozzle of the engine. In [13,14], a vector quad-rotor was proposed in which the engine was rotated along two axes to achieve zero-pitch-angle flight of the aircraft in a redundant manner. However, the engine weight was large, which imposed higher requirements on the tilting mechanism. Moreover, tilting the engine disrupted the streamlines of the fuselage and increased the resistance during cruising. The Russian Jacques-38 and Jacques-141 are VTOL aircraft that use a combination of lift engines and deflected main engine nozzles [15]. In this layout, the lift engine occupies a large space in the fuselage, and the engine is not used during cruise flight. Vectoring nozzles are the key to engine thrust vectoring technology, which can, in principle, be divided into mechanical regulation, plasma jet regulation, and pneumatic jet regulation. Among them, the mechanical regulation of the vectoring nozzle is the most mature and widely used. A novel large-deflection-angle thrust vectoring nozzle called ACHEON was adopted, and a complete self-position control scheme for this type of fixed-wing UAV with thrust vectoring was developed in [16]. In [17], the thrust vectoring nozzle was controlled by the steering gear, which could deflect the pitching and yawing directions. The installation positions of the connecting rods of the two channels were orthogonal, which eliminated the coupling motion between the pitching and yawing channels. In addition, flaps with an airfoil were placed in the nozzle outlet of the ducted fan, and the attitude control was generated by changing the angle of attack of the flaps in [18]. However, the nozzle rotation angle was limited, and when the engine was perpendicular to the surface of the fuselage, it increased the difficulty of the design of the streamline of the VTOL aircraft.

In terms of attitude assistance control, the F35B adopts a vertical thrust system, which can generate lift force during takeoff. It also leads the compression of air generated by the engine to the wings on both sides, and it is possible to adjust the direction and volume of the jet exhaust to control the attitude of the aircraft during take-off or landing. Additional electric ducted fans were introduced to assist in the attitude control in [19]. A Pegasus-type thrust steering engine was installed in the middle of the Harrier fuselage [20]. In the front and rear, two pairs of rotatable nozzles were located on both sides of the fuselage. They could be rotated from 0° to 98° [21] and were symmetrical with respect to the center of gravity of the fuselage. As the four nozzles must be linked, and the resultant force of the thrust generated by the four nozzles is always required to pass through the center of the gravity of the aircraft, the Harrier was equipped with three pairs of attitude control nozzles. According to [13], a fixed engine thrust was selected, and attitude control was performed by using a two-dimensional vector method. The above methods made the structure of the aircraft more complicated.

In order to solve the problem of the slow speed response of turbojet engines, we designed one-dimensional thrust vectoring nozzle modules that arranged the turbojet engine horizontally and rotated the nozzle from horizontal to vertical positions. In the process of downward rotation of the nozzle, the direct blowing of the turbojet engine on the ground was prevented, which reduced the ground effect. Referring to the design of the guide vane in two references [22,23], the nozzle with an arc-shaped guide vane had a more uniform airflow streamline and better thrust efficiency. The thrust distribution characteristics of one-dimensional vector nozzle modules and the thrust change process during the nozzle rotation were obtained. The thrust of the engine was fixed, and the thrust difference caused by the difference between the angles of multiple vector nozzles was used for attitude stability control, which reduced the difficulty of control.

The rest of this paper is organized as follows. The structure of the one-dimensional thrust vectoring nozzle modules is introduced in Section 2. The computational fluid dynamics (CFD) simulations and experimental tests conducted in this study are described

in Section 3. The control strategy of a one-dimensional thrust vectoring nozzle turbojet aircraft and the results of the simulations are discussed in Section 4. Section 5 presents the experimental results, and conclusions are drawn in Section 6.

2. Hardware

As shown in Figure 1, the mechanical design of our aircraft consisted of two main parts: (i) a central rigid body that carried the fuel tanks, batteries, sensors, and control systems required for flight and (ii) four one-dimensional thrust vectoring nozzle modules. The choice of four modules represented a compromise between simplicity and the ability to generate enough thrust to compensate for gravity, with an associated mechanical complexity that could result in a bulky drone with limited flight time and payload. Each one-dimensional thrust vectoring nozzle module included a turbojet engine, a rotating pair of modules composed of nozzles and bearings, and a four-bar linkage that drove by using the steering gear.

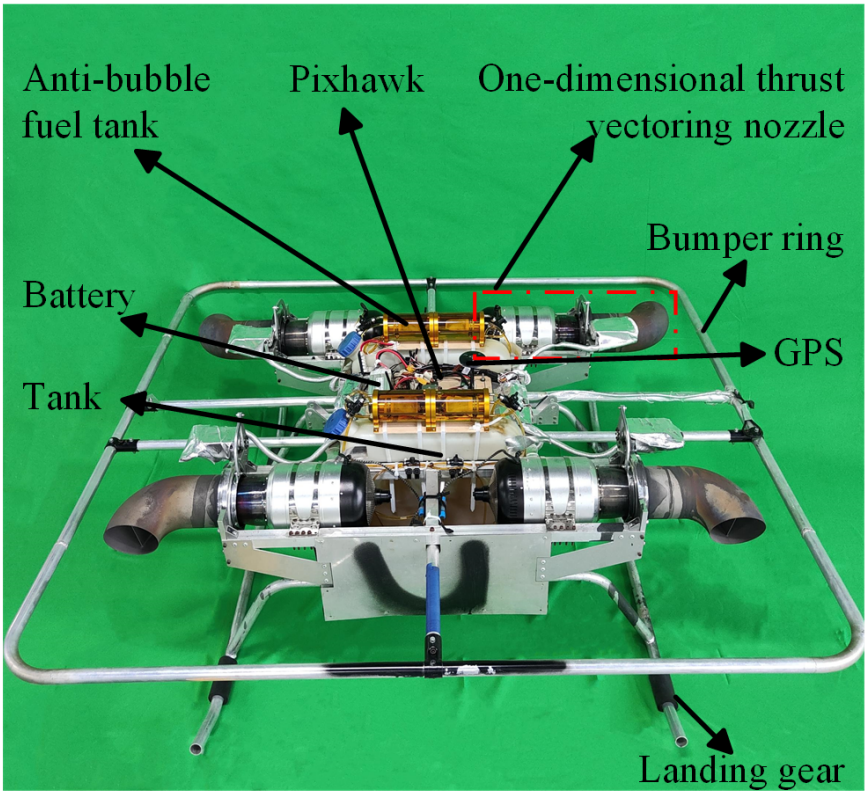

Figure 1. One-dimensional vector turbojet aircraft.

As shown in Figure 2, the nozzle was fixed to the rear of the turbojet through structural parts such as bearings, the axis of the turbojet engine coincided with the axis of the bearing, and the airflow generated by the turbojet was turned through the nozzle. The crank–rocker mechanism, which comprised crank 1 and rocker 2, could realize one-dimensional rotation with a steering-gear driving nozzle. A rotation range of no more than 180° could be achieved by adjusting the length of the four-link rod. To avoid a singularity of the four-bar linkage mechanism, the rotation range here was selected as 90°.

To improve the load capacity of the VTOL aircraft, an engine with a high thrust-to-weight ratio was needed. The SWIWIN SW400Pro turbojet engine was selected here; it can provide a maximum thrust of 400 N. To improve the stability of the vector system, the KST HS25-30-M-5545-1 A steering gear was selected. Table 1 shows the complete list of electronic components included in this platform.

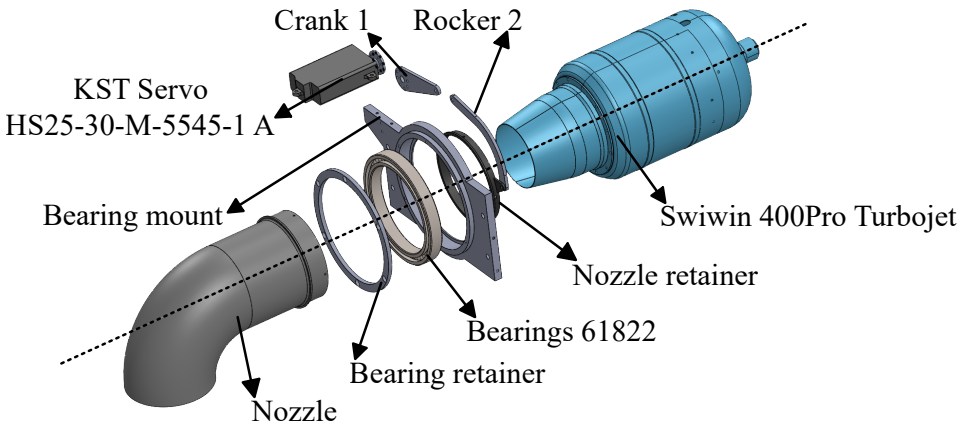

Figure 2. One-dimensional thrust vectoring nozzle explosion diagram.

Table 1. Electronic components included in the aircraft.

Component	Name
Turbojet	SWIWIN SW400Pro
servo	KST HS25-30-M-5545-1 A
Battery	Grepow Lipo 4s
BEC 5v	Hobby wing UBEC
Flight controller	Pixhawk
RC receiver	Futaba R3008SB

3. Study of Nozzle Characteristics

The presence of the nozzle changed the direction of the high-speed airflow generated by the turbojet. The airflow along the axial direction turned along the radial direction of the engine. Due to the obstruction and wear of the nozzle, its force efficiency on the airflow decreased. The force characteristics of the one-dimensional thrust vectoring nozzle module were related to the stability of the aircraft. The thrust distribution during the nozzle rotation was essential for modeling the aircraft. As shown in Figure 3, the diameter of nozzle D, the length of the straight pipe section L, the end angle α, and the presence or absence of guide vanes all affected the high-speed airflow generated by the turbojet engine. The arc-shaped guide vane was at 95° with a thickness of 3 mm. To determine the impact of the nozzle, a CFD simulation and experimental analysis were conducted.

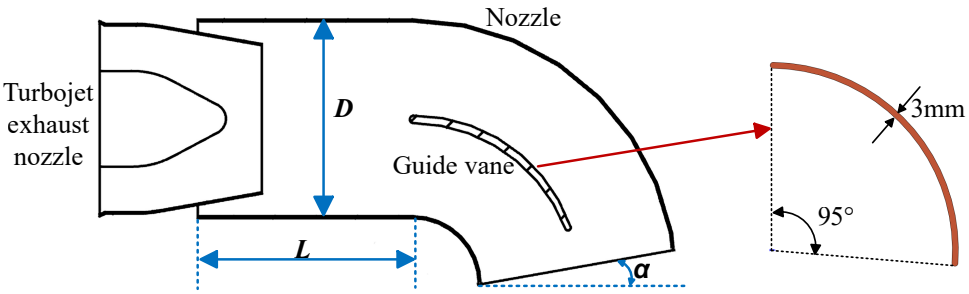

Figure 3. Design parameters of the nozzle structure.

3.1. CFD Simulation Analysis

We focused on the viscous compressible turbulent motion of the high-speed airflow generated by the turbojet in the nozzle; thus, the gravitational effect, thermal radiation, chemical reaction, and the influence of the airflow before the nozzle of the turbojet were neglected in the computational domain. The Reynolds-averaged Navier–Stokes (RANS) formulations with the corresponding turbulence closures are the preferred methods—particularly in industry—for the analysis of compressible turbulent jet flows. Within this

framework, two-equation turbulence models are used the most. SST k-ω had a major improvement in performance over both the original k-ω and the standard k-ε model [24]. The turbulent viscosity, which was modified to account for the transport of the principal turbulent shear stress, gave it an advantage in terms of performance over both the standard k-ω and k-ε formulations. It behaved as a k-ω model in the inner region of the boundary layers and as a k-ε model in the outer region of the boundary layers, in the free-stream zones. The authors of [25] proved the capabilities of the SST k-ω turbulence model within the steady-state RANS formulation for predicting a high-subsonic, coaxial-heated jet issued from a bypass ratio of a five-turbofan engine model, which was consistent with our cases.

The structured mesh was divided by using Fluent meshing. The far-field of the nozzle outlet was cylindrical, the distance from the axis of the nozzle outlet was 40 times the nozzle radius, and the nozzle extended 20 times the distance of the radius in the circumferential direction. After encrypting the grids at the nozzle wall, the grid independence check was performed. For the same example, we divided the number of grids into 8.27×10^6 and 1.52×10^7, respectively, and the calculated results were consistent. The calculated results are shown in Table 2. As the nozzles calculated in the simulations had different dimensions, the grid numbers differ from 7×10^6 to 9×10^6.

Table 2. Data from the grid independence check.

	Grid Number	Mass Flow at Nozzle Outlet	Velocity of Nozzle Outlet	Thrust Turning Angle
Case 1	8.27×10^6	0.978	331.14 m/s	79.17°
Case 2	1.52×10^7	0.980	331.63 m/s	79.16°

Referring to the settings of the methods in [25], the compressible flow simulations were carried out by using a pressure-based solver. For the RANS simulations, the pressure–velocity coupling was achieved through the Coupled scheme, which provided superior performance compared with the segregated scheme for steady-state flows. Second-order upwind finite-volume schemes were employed for the spatial discretization of the terms in the RANS equations. The specific values of the model boundary conditions were set as follows: The total pressure of the nozzle inlet was 1053 K, the total pressure was 1.446×10^5 Pa, the back pressure of the nozzle outlet interface was 1.0×10^5 Pa, the external far-field static pressure was 1.0×10^5 Pa, and the total temperature was fixed at 300 K.

The thrust calculation method was $F = mv + A(P_n - P_0)$, where m is the gas mass flow rate, v is the outlet gas velocity, A is the outlet area, P_n is the outlet static pressure, and P_0 is the outside atmospheric pressure. According to the simulation results, the turbojet thrust was 362.743 N. Figure 4 shows the effects of different nozzle modules on the thrust. As shown in Figure 4a, when L gradually increased to 140 mm, F_y increased to the maximum value of 317.183 N, and then the thrust decreased, with L increasing gradually. Figure 4b shows that F_y gradually decreased and F_z gradually increased as the angle α increased. Figure 4c shows that the thrusts in the Y and Z directions improved due to the guide vane. Figure 4d shows that the presence of the guide vane made the airflow distribution more uniform. In summary, the nozzle with an arc-shaped guide vane had the best thrust efficiency with the appropriate straight pipe length L and an angle equal to zero.

3.2. Nozzle Test Analysis

To validate the simulation results, different nozzles were printed and tested. From the simulation results, we were able to find that increasing the pipe length L improved the thrust, but also increased the aircraft volume and weight. As a comparison, we set L to 60 and 80 mm, α to 0° and 10°, and the presence or absence of an arc-shaped guide vane. As shown in Figure 5, we printed nozzles in four sizes, and their detailed sizes are shown in Table 3. We built an experimental platform based on a six-dimensional force balance, as shown in Figure 6. Full-throttle thrust tests were conducted in the same environment (0 °C, 50 m above sea level), and the force test results are shown in Table 3.

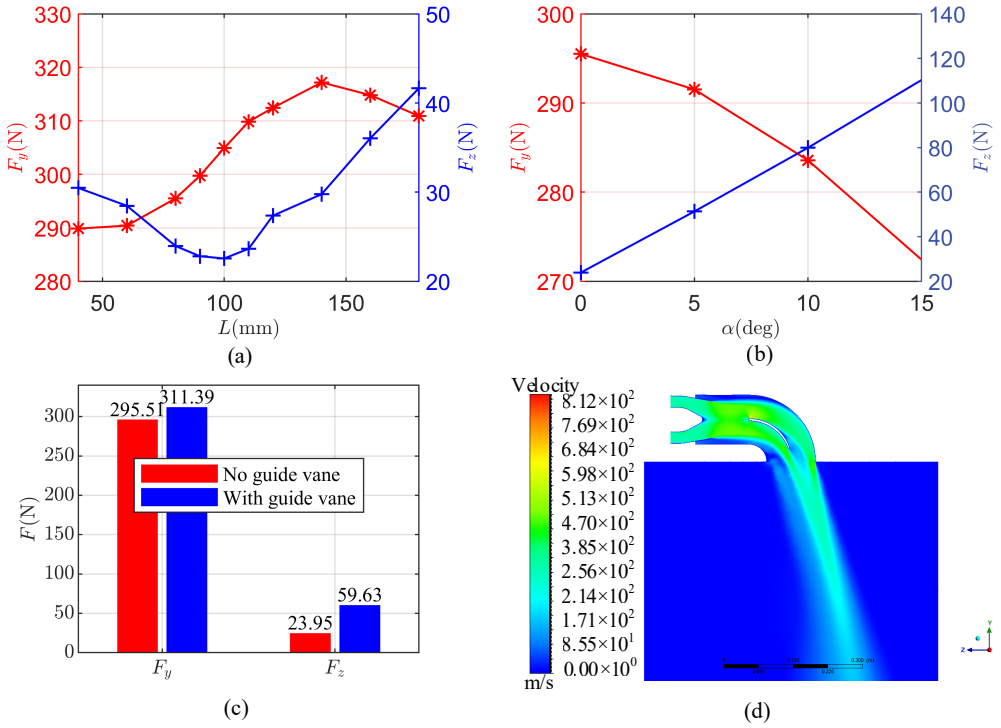

Figure 4. Effects of the nozzle parameters on the thrust in the simulation: (**a**) effect of the length L on the thrust; (**b**) effect of the angle α on the thrust; (**c**) effect of the guide vane on the thrust; (**d**) description of the guide vane's influence the distribution of air flow.

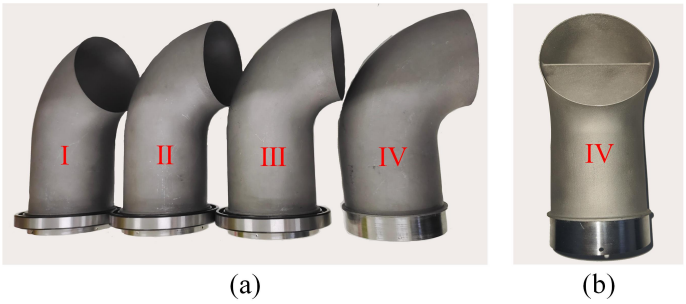

Figure 5. The 3D-printed nozzles: (**a**) four sizes of nozzles; (**b**) right view of nozzle IV.

Table 3. Nozzle size parameters and force test results.

	L	α	Guide Vane	F_x	F_y	F_z
No nozzles	-	-	-	2.82 N	404.70 N	0.39 N
Nozzle I	60 mm	0°	no	323.59 N	59.44 N	1.71 N
Nozzle II	80 mm	10°	no	318.75 N	126.60 N	1.86 N
Nozzle III	80 mm	0°	no	333.26 N	62.27 N	1.26 N
Nozzle IV	80 mm	0°	yes	343.69 N	86.21 N	1.83 N

In the comparison with the simulation results, the experiments and simulations showed the same trends when the structural parameters of the different nozzles changed. Nozzle IV, which had an arc-shaped guide vane, L of 80 mm, and α of 0°, had a higher efficiency (87.56%) compared with that of the turbojet engine. Thus, nozzle IV was used in the aircraft.

In order to confirm how the thrust changed during the rotation of the nozzle, the nozzle was driven by a steering gear, as shown in Figure 6, and changes in the force were recorded. The experimental results are shown in Figure 7. The forces along the axial direction of the turbojet (F_y) remained at 125 N during the rotation of the nozzle. F_x and F_z, which were distributed in the nozzle rotation plane, were a trigonometric function of the nozzle angle. The total thrust through the nozzle remained 340 N.

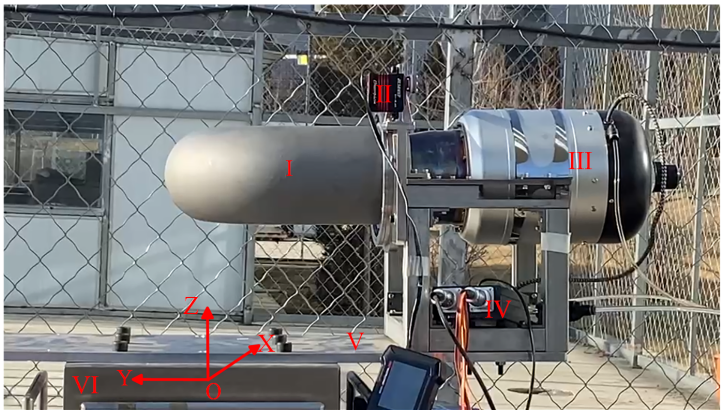

Figure 6. Experimental platform with a six-dimensional force balance. I: Nozzle; II: steering gear; III: turbojet; IV: ECU; V: connecting plate; VI: six-dimensional force balance.

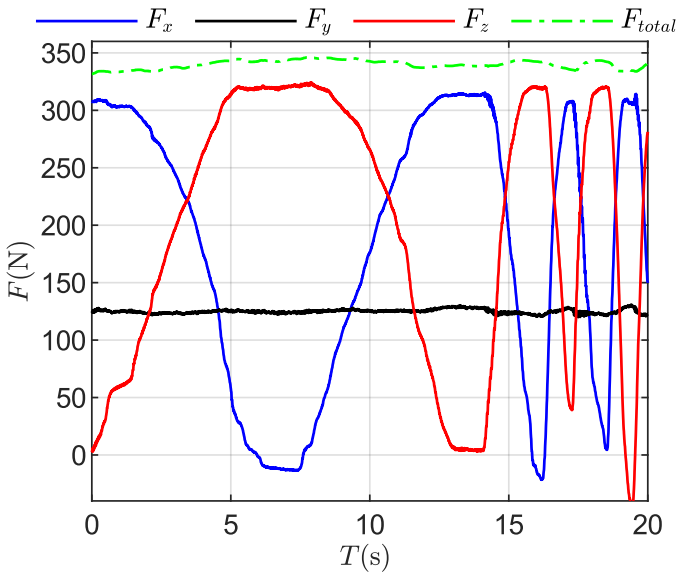

Figure 7. Force change during the rotation of the nozzle.

4. Modeling and Control

4.1. Attitude Control Strategy

After obtaining the force variation characteristics of the one-dimensional thrust vectoring nozzle module, we analyzed how the position and attitude of the aircraft could be controlled by using the force and moment generated by the modules; this analysis is described in this section. We kept the turbojet at the same throttle and used the rotation of the nozzle to control the thrust because of the slow speed response of the turbojet. As shown in Section 3, although there were forces along the axial direction of the one-dimensional thrust vectoring nozzle module, the modules were placed symmetrically in the aircraft, and the forces along the Y-axis of the aircraft offset each other. Then, the thrust was divided along the XZ-plane, where $F_{i1}(i = 1, 2, 3, 4)$ was along the Z-axis and $F_{i2}(i = 1, 2, 3, 4)$ was

along the X-axis of the body. The way of using the force distribution to realize attitude control is shown in Figure 8.

$$\begin{cases} F_{i1} = F_i cos\delta_i \\ F_{i2} = F_i sin\delta_i \\ F_1 = F_2 = F_3 = F_4 \end{cases} \quad (1)$$

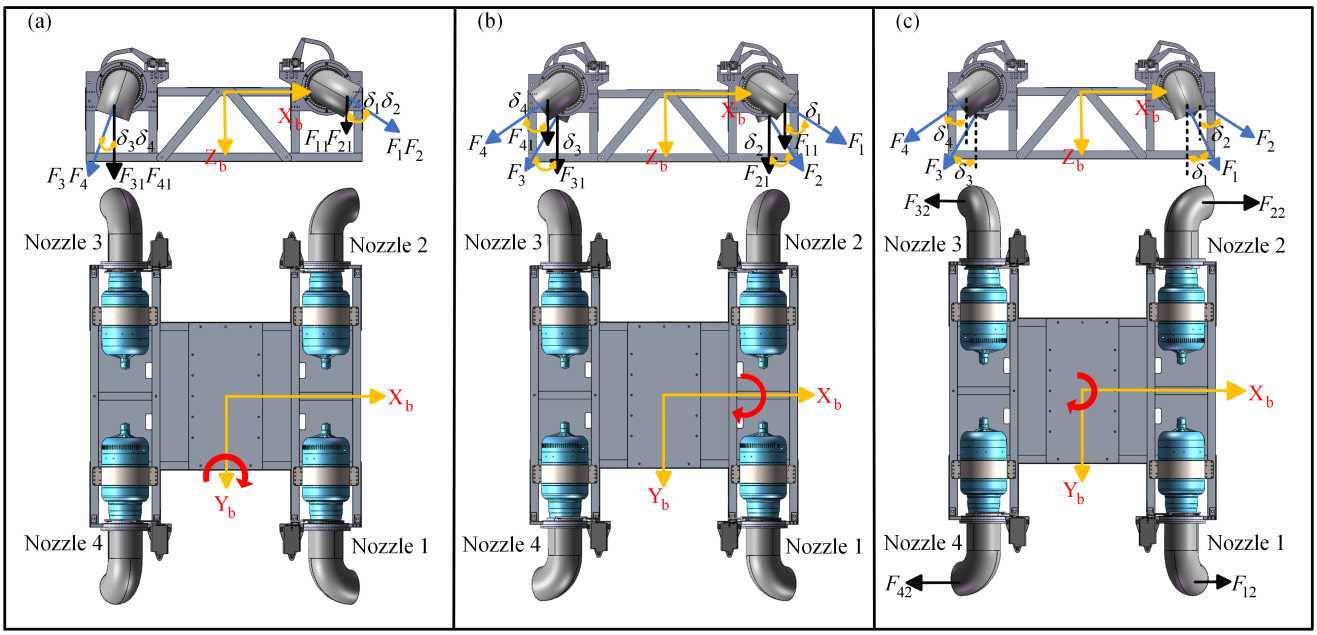

Figure 8. Attitude control schematic: (**a**) nozzles motion to produce pitch angular acceleration; (**b**) nozzles motion to produce roll angular acceleration; (**c**) nozzles motion to produce yaw angular acceleration.

Figure 8a shows how the aircraft realized pitch. When $\delta_1 = \delta_2 > \delta_3 = \delta_4$, the force followed Equation (2) and generated positive torque around the Y-axis of the body, and the aircraft had positive pitch acceleration. In contrast, when $\delta_1 = \delta_2 < \delta_3 = \delta_4$, it generated negative torque, and the aircraft had negative pitch acceleration. Notably, as the thrust was fixed, $\sum_{i=1}^{4} F_{i2} \neq 0$ and $\sum_{i=1}^{4} F_{i2}$ were regarded as disturbances.

$$\begin{cases} \sum_{i=1}^{4} F_{i1} = mg \\ F_{31} = F_{41} > F_{11} = F_{21} \end{cases} \quad (2)$$

Figure 8b shows how the aircraft realized roll. When $\delta_1 = \delta_4 > \delta_2 = \delta_3$, the force followed Equation (3) and generated positive torque around the X-axis of the body; the aircraft had positive roll acceleration. In contrast, when $\delta_1 = \delta_4 < \delta_2 = \delta_3$, it generated negative torque, and the aircraft had negative roll acceleration.

$$\begin{cases} \sum_{i=1}^{4} F_{i1} = mg \\ \sum_{i=1}^{4} F_{i2} = 0 \\ F_{21} = F_{31} > F_{11} = F_{41} \end{cases} \quad (3)$$

Figure 8c shows how the aircraft realized yaw. When $\delta_2 = \delta_4 > \delta_1 = \delta_3$, the force followed Equation (4) and generated positive torque around the Z-axis of the body; the

aircraft had positive yaw acceleration. In contrast, when $\delta_2 = \delta_4 < \delta_1 = \delta_3$, it generated negative torque, and the aircraft had negative yaw acceleration.

$$\begin{cases} \sum_{i=1}^{4} F_{i1} = mg \\ \sum_{i=1}^{4} F_{i2} = 0 \\ F_{22} = F_{42} > F_{12} = F_{32} \end{cases} \tag{4}$$

4.2. Modeling of the Aircraft

The following assumptions were introduced to simplify the airframe model: It was considered that the aircraft was a rigid symmetric structure and that no structural deformation occurred during flight; the airflows of the turbojets did not interfere with each other, and the thrust values of the four turbojets were identical when they had same throttle; changes in mass and moment of inertia were ignored. The mass change was caused by fuel consumption, which was uniform and continuous. As the fuel tank was designed to be in the center of the aircraft, near the center of mass, the moment of inertia changed slowly. As the aircraft had sufficient control force and torque, we used the initial mass and moment of inertia.

The inertial frame $\boldsymbol{E}$ was fixed on the ground, and its z-axis pointed upward. In contrast, the z-axis of the body frame $\boldsymbol{B}$ pointed downward, as shown in Figure 9; its origin was at the center of gravity. The symbols are listed in Table 4. $\boldsymbol{R}_{\boldsymbol{B}}^{\boldsymbol{E}}$ defined the transformation matrix that allowed the transformation of a vector from the body-fixed frame to the inertial frame, where $s(\cdot)$ and $c(\cdot)$ are the $sin(\cdot)$ and $cos(\cdot)$ of a given angle, respectively.

$$\boldsymbol{R}_{\boldsymbol{B}}^{\boldsymbol{E}} = \begin{bmatrix} c_\theta c_\psi & s_\phi s_\theta c_\psi - c_\phi s_\psi & c_\phi s_\theta c_\psi + s_\phi s_\psi \\ c_\theta s_\psi & s_\phi s_\theta s_\psi + c_\phi c_\psi & c_\phi s_\theta s_\psi - s_\phi c_\psi \\ -s_\theta & s_\phi c_\theta & c_\phi c_\theta \end{bmatrix} \tag{5}$$

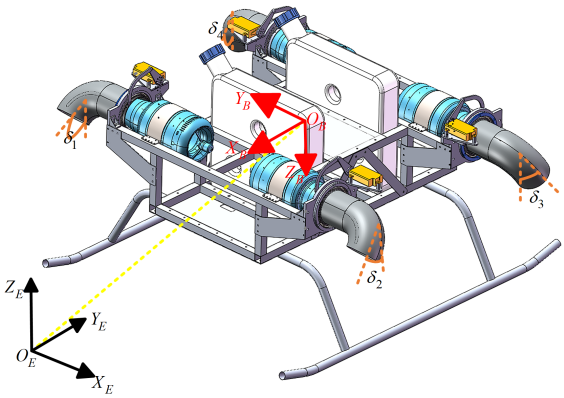

Figure 9. The inertial and body coordinate systems.

$\dot{\boldsymbol{\eta}} = [\dot{\phi}, \dot{\theta}, \dot{\psi}]^T$ represents the attitude angular velocity coordinates in the Earth coordinate system, and $\boldsymbol{\omega_B} = [p, q, r]^T$ represents the corresponding attitude angular velocity coordinates in the body coordinate system. According to the coordinate transformation matrix $\boldsymbol{R}_{\boldsymbol{B}}^{\boldsymbol{E}}$, the relationship between $\dot{\boldsymbol{\eta}}$ and $\boldsymbol{\omega_B}$ is described as follows, where $s(\cdot)$ and $c(\cdot)$ are the $sin(\cdot)$ and $cos(\cdot)$ of a given angle, respectively:

$$\boldsymbol{\omega_B} = \begin{bmatrix} 1 & 0 & -s_\theta \\ 0 & c_\phi & c_\theta s_\phi \\ 0 & -s_\phi & c_\theta c_\phi \end{bmatrix} \dot{\boldsymbol{\eta}} \tag{6}$$

Table 4. Meanings of symbols.

Symbol	Meanings
$\boldsymbol{E} = \{O_E, x_e, y_e, z_e\}$	inertial reference frame
$\boldsymbol{B} = \{O_B, x_b, y_b, z_b\}$	body-fixed reference frame
$\boldsymbol{\xi} = [x, y, z]^T$	position in the inertial system
$\boldsymbol{\eta} = [\phi, \theta, \psi]^T$	attitude under the inertial system
$\boldsymbol{\omega_B} = [p, q, r]^T$	angular velocity in the body-fixed system
$\boldsymbol{I} = \text{diag}[I_{xx}, I_{yy}, I_{zz}]$	moment of inertia along the body axis
$\boldsymbol{F_d} = [F_{dx}, F_{dy}, F_{dz}]$	wind resistance forces
$\boldsymbol{\tau_d} = [\tau_{dx}, \tau_{dy}, \tau_{dz}]$	resistance torque
$\delta_i (i = 1, 2, 3, 4)$	rotation angle of the i-th nozzle
l_1, l_2	distance between the thrust center and centroid
m	aircraft mass

In Section 3, the forces along the axial direction of the turbojet remained unchanged during the rotation of the nozzle. As the one-dimensional thrust vectoring nozzle modules were placed symmetrically on the aircraft, the resultant force along the aircraft's Y-axis was offset to zero. The force produced by the one-dimensional thrust vectoring nozzle module was distributed in the X- and Z-directions relative to the aircraft; its resultant force was T. For the modeling of the body dynamics, the Newton–Euler formalism [26] was used. $\boldsymbol{F}$ and $\boldsymbol{\tau_b}$ represented the thrust and moment separately generated by the aircraft, $\boldsymbol{F_g}$ represented the gravity, $\boldsymbol{F_d}$ represented the wind resistance force, and $\boldsymbol{\tau_d}$ represented the resistance torque. The general form is the following:

$$\begin{cases} m\ddot{\boldsymbol{\xi}} = \boldsymbol{R_B^E F} - \boldsymbol{F_g} - \boldsymbol{F_d} \\ \boldsymbol{I\dot{\omega}_B} = \boldsymbol{\tau_b} - \boldsymbol{\omega_B^T} \times \boldsymbol{I\omega_B} - \boldsymbol{\tau_d} \end{cases} \tag{7}$$

The forces and moments produced by the aircraft are the following:

$$\boldsymbol{F} = \begin{bmatrix} Tsin\delta_1 + Tsin\delta_2 - Tsin\delta_3 - Tsin\delta_4 \\ 0 \\ Tcos\delta_1 + Tcos\delta_2 + Tcos\delta_3 + Tcos\delta_4 \end{bmatrix} \tag{8}$$

$$\boldsymbol{\tau_b} = \begin{bmatrix} l_1(Tcos\delta_1 + Tcos\delta_2 - Tcos\delta_3 - Tcos\delta_4) \\ l_2(-Tcos\delta_1 + Tcos\delta_2 + Tcos\delta_3 - Tcos\delta_4) \\ l_1(Tsin\delta_1 - Tsin\delta_2 + Tsin\delta_3 - Tsin\delta_4) \end{bmatrix} \tag{9}$$

$C = [c_x, c_y, c_z]^T$ is a positive constant matrix. The gravity and wind resistance are described as follows:

$$\boldsymbol{F_g} = \begin{bmatrix} 0 \\ 0 \\ mg \end{bmatrix} \tag{10}$$

$$\boldsymbol{F_d} = C\dot{\xi} = \begin{bmatrix} c_x\dot{x} \\ c_y\dot{y} \\ c_z\dot{z} \end{bmatrix} \tag{11}$$

4.3. Position and Attitude Control

The input was the rotation angle of the four nozzles, and the output was the three-axis position and attitude, which comprised an underactuated system. Since the output of the model was more than the input, not all outputs could be controlled independently. The aircraft was controlled by a cascade control structure, and the outermost control loop was the position controller. This control method was called time-scale separation, which worked as long as the inner loop was much faster than the outer loop. The position loop and attitude loop were controlled by cascade PIDs.

The position error is defined as the difference between the desired and estimated position $\boldsymbol{\xi_{err}} = \boldsymbol{\xi_{des}} - \boldsymbol{\xi}$. The position control law is given by Equation (12), where $k_{p,p}$, $k_{i,p}$, and $k_{d,p}$ are the proportional, derivative, and integral gains, respectively. The desired attitude angles are given by Equations (13) and (14).

$$\boldsymbol{a_{des}} = k_{p,p}\dot{\boldsymbol{\xi}}_{\boldsymbol{err}} + k_{i,p}\int \dot{\boldsymbol{\xi}}_{\boldsymbol{err}}dt + k_{d,p}\ddot{\boldsymbol{\xi}}_{\boldsymbol{err}} \tag{12}$$

$$\phi_{des} = -arctan\frac{\boldsymbol{a_{des}}(1) \times sin\psi + \boldsymbol{a_{des}}(2) \times cos\psi}{g} \tag{13}$$

$$\theta_{des} = arctan\frac{\boldsymbol{a_{des}}(1) \times cos\psi + \boldsymbol{a_{des}}(2) \times sin\psi}{g} \tag{14}$$

The attitude error is defined as the difference between the desired and estimated attitude angles $\boldsymbol{\eta_{err}} = \boldsymbol{\eta_{des}} - \boldsymbol{\eta}$. The attitude control law is given by Equation (15), where $k_{p,a}$, $k_{i,a}$, and $k_{d,a}$ are the proportional, derivative, and integral gains, respectively.

$$\boldsymbol{w_{des}} = k_{p,a}\dot{\boldsymbol{\eta}}_{\boldsymbol{err}} + k_{i,a}\int \dot{\boldsymbol{\eta}}_{\boldsymbol{err}}dt + k_{d,a}\ddot{\boldsymbol{\eta}}_{\boldsymbol{err}} \tag{15}$$

5. Simulation

Our proposed attitude control strategy is verified with a simulation in this section. MATLAB and Flight-Gear co-simulations were conducted; the dynamic model and controller of the aircraft were built in MATLAB, the route navigation was performed by Flight-Gear, and the control frequency was 100 Hz, which did not exceed the PX4 control frequency. The aircraft parameters are specified in Table 5.

Table 5. Parameters of the aircraft model.

Parameter	Value
m	61 kg
I_{xx}	4.7 kg·m^2
I_{yy}	5.7 kg·m^2
I_{zz}	9.2 kg·m^2
l_1	1.128 m
l_2	0.630 m
g	9.8 m·s^{-2}
T	21 kgf

Trajectory tracking is the first simulation purpose to be examined when there are uncertainties in a system. The results are presented for the designed controllers to display the effectiveness of the new control form. The step signals at 0–5 m along the Z-, X-, and Y-axes in the inertial reference frame were given in Simulink, and then the aircraft flew back over the takeoff point and landed on the origin of the inertial reference. Then, the desired coordinate point at the next moment was given by the Flight-Gear software; the "Earth–North–Up"(ENU) coordinate system was adopted, and the desired trajectory and the actual trajectory are shown in Figure 10a. As shown in Figure 10b, the position tracking errors were within 0.1 m, and Figure 11 shows the velocity responses. There was an approximately 10% overshoot of velocity. The position loop was affected by the attitude loop, which was the inner loop of the position loop. Figure 12 shows that the rolling angle of the aircraft was basically zero, and there was only a slight fluctuation during the disturbance. As a change in the pitch angle corresponded to a change in the aircraft speed and a change in the yaw angles corresponded to a change in the flight path, the aircraft changed course by yawing and used pitch to control flight speed. Since the actuators needed a certain amount of time to respond, there was a phase delay of 0.2 s. The simulation results showed that the

aircraft had a good position and attitude tracking ability, thus proving the effectiveness of the designed control method and controller.

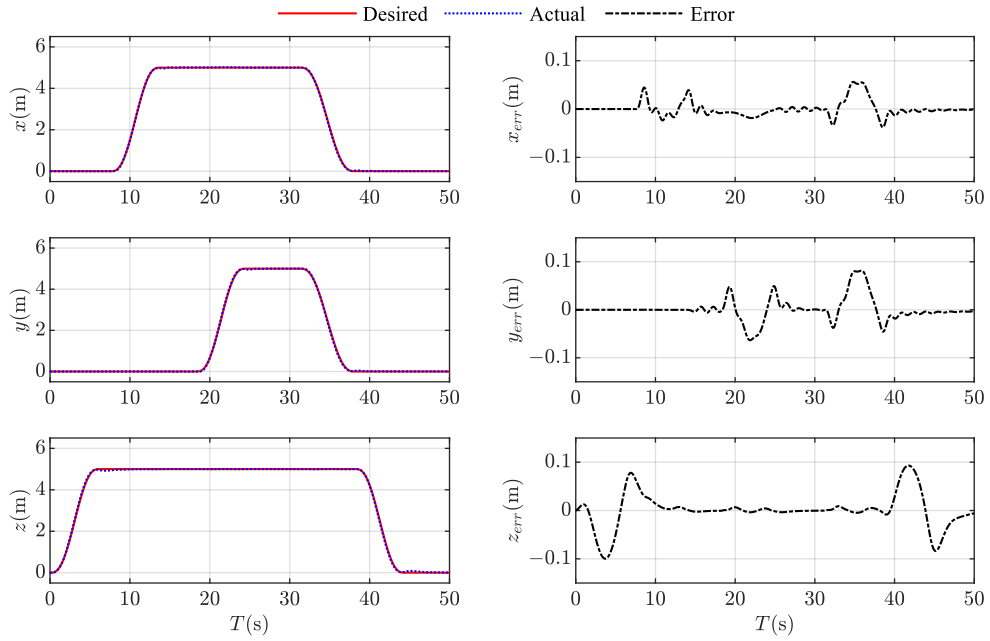

(**a**) (**b**)

Figure 10. Position tracking in the simulation: (**a**) position tracking response; (**b**) position tracking error.

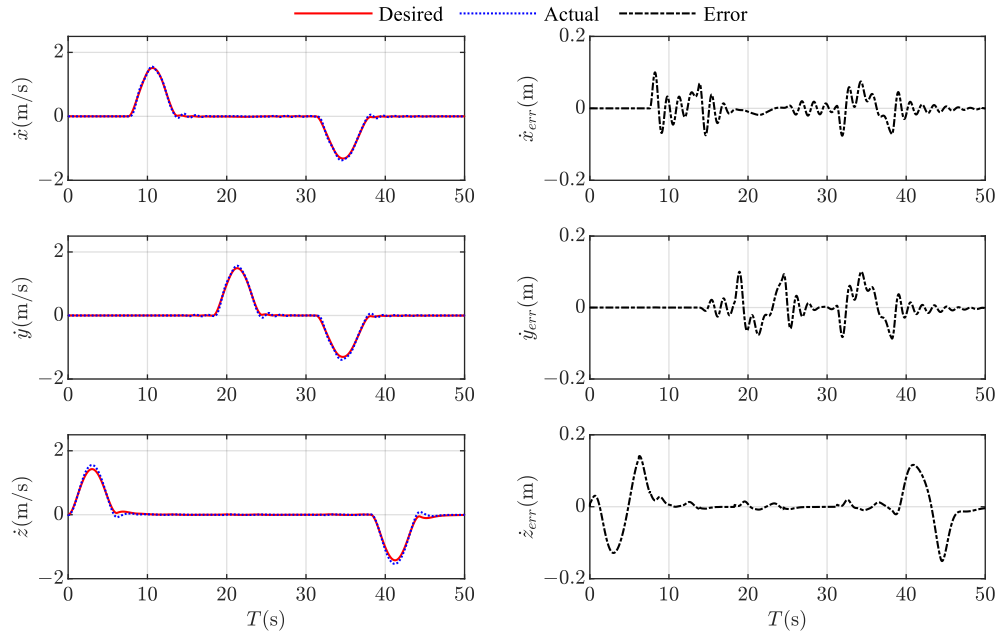

(**a**) (**b**)

Figure 11. Velocity tracking in the simulation: (**a**) velocity tracking response; (**b**) velocity tracking error.

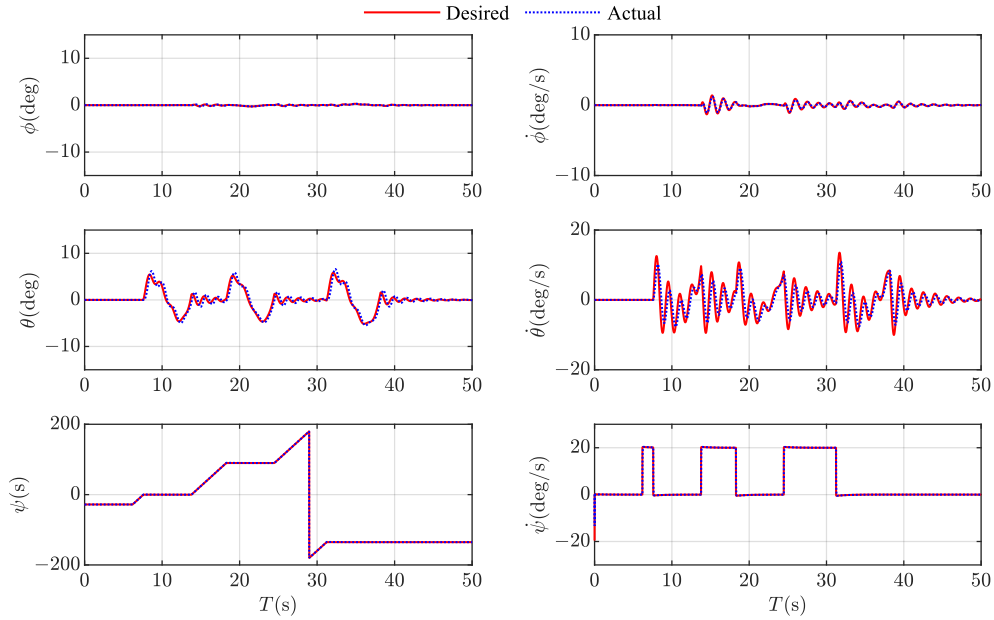

(**a**) (**b**)

Figure 12. Attitude tracking in the simulation: (**a**) attitude angle tracking response; (**b**) attitude angle velocity tracking response.

The change process of the nozzles' angles during the flight simulation is recorded in Figure 13. By comparing the change in the nozzle angles with the flight intentions, we found that: there existed a hover nozzle angle δ_g for which the resultant force along the vertical direction was equal to gravity, and the aircraft hovered when the four nozzles' angles were equal to δ_g; the aircraft had upward acceleration when the angles of the nozzles were smaller than δ_g, and the aircraft had downward acceleration when the angles of the nozzles were greater than δ_g; the aircraft had positive yaw acceleration when the angles of nozzle 1 and nozzle 3 were smaller than δ_g and the angles of nozzle 2 and nozzle 4 were greater than δ_g; the aircraft had negative pitch acceleration when the angles of nozzle 1 and nozzle 2 were smaller than δ_g and the angles of nozzle 3 and nozzle 4 were greater than δ_g; the aircraft had positive roll acceleration when the angles of nozzle 2 and nozzle 3 were smaller than δ_g and the angles of nozzle 1 and nozzle 4 were greater than δ_g. These changes were consistent with the control schematic shown in Figure 8.

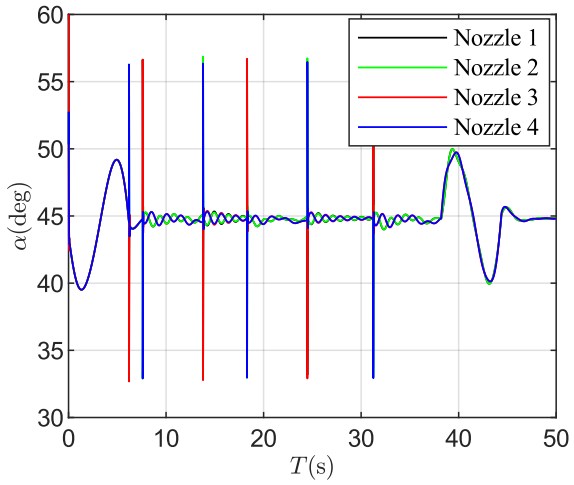

Figure 13. Changes in the nozzle angles in the simulation.

As mentioned above, $\sum_{i=1}^{4} F_{i2} \neq 0$ when the aircraft pitched. We recorded the resultant force along the X-axis of the aircraft that was generated by the four turbojet engines during the simulation, as shown in Figure 14. We found that the resultant force was less than 10 N. As discussed in Section 4.1, the angles of nozzle 1 and nozzle 2 were different from those of nozzle 3 and nozzle 4 when the aircraft pitched, so the resultant force along the aircraft X-axis was not zero. The angle difference between the nozzles was larger due to the larger pitch angle acceleration, which caused a larger resultant force along the aircraft's X-axis.

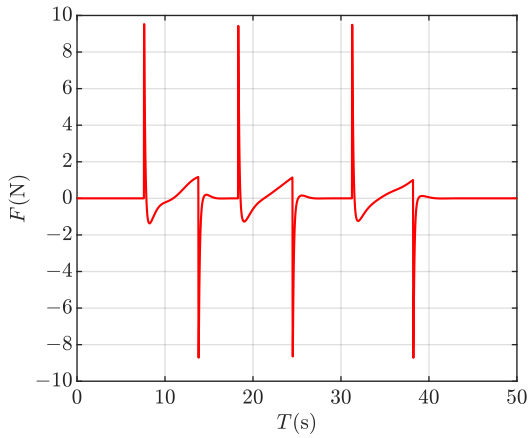

Figure 14. Disturbance force along the X-direction of the aircraft.

6. Experiment

In this section, trajectory tracking experiments on an outdoor aircraft are presented in order to illustrate the effectiveness of the proposed control schematic. The experimental prototype is shown in Figure 1. The position and attitude information of the aircraft were obtained by sensors integrated into pixhawk. The information collected by the sensors was filtered and fused by using EKF2 and then fed to the pose controller. The "North–East–Down" (NED) coordinate system was adopted; Figure 15 shows the desired and actual three-dimensional trajectories, and Figure 16 displays the aircraft attitude changes in sequence during the turn marked in Figure 15. During the flight, the turbojet speed was fixed at 90,000 rpm, corresponding to 30 kgf at 15 °C, and 25 m above sea level. The onboard fuel capacity was 20 L, and the endurance was about five minutes. The outdoor temperature of the test environment was 20 °C and the wind speed was around 0–1 m/s, 50 m above sea level. The initial mass of the aircraft was 61 kg, and its dimensions were consistent with those in the simulation.

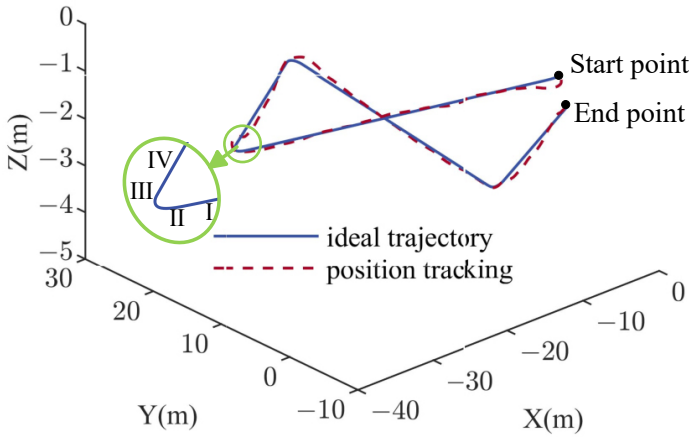

Figure 15. Three-dimensional trajectories of the aircraft.

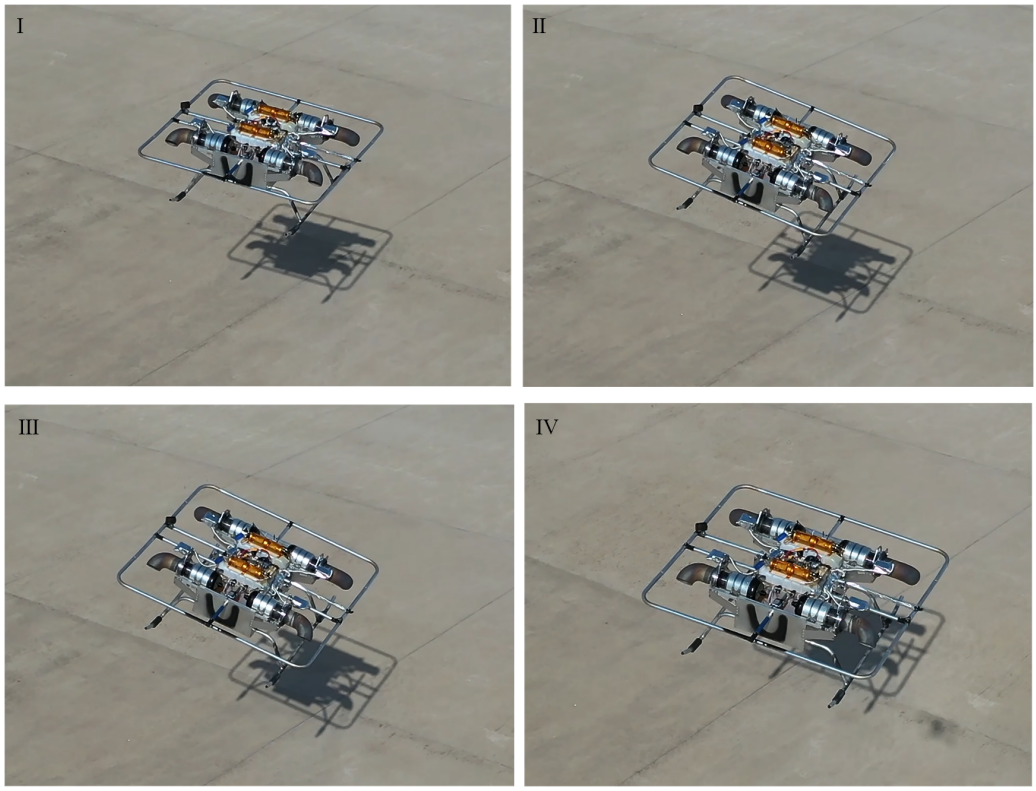

Figure 16. Change in the attitude of the aircraft during the tuning process.

The simulation proved that the aircraft could turn by using the yaw; in order to ensure the safety of the flight process and show the aircraft had a wide range of adaptability, as shown in Figure 17a, we kept the yaw angle unchanged during the course of flight and relied on tilting the fuselage to change direction. With reference to Figures 16 and 17, the turning process shown in Figure 16 corresponded to the period of 17–20 s in Figure 17, where the pitch angle and roll angle changed in coordination to complete the turning process. The direction of forward flight was changed at an obtuse angle during the turning phase; thus, the aircraft completed the turning operation with a large roll angle and a small pitch angle. Corresponding to Figure 18, $\dot{x}$ changed from -2 to 2 m/s, and in Figure 17, the direction of movement changed along the X-axis during the period of 17–20 s. In Figure 17a, there are five major changes in the pitch angle and roll angle. The first and last changes corresponded to the acceleration from the start point and deceleration before reaching the endpoint, and the middle three changes corresponded to the three turns in Figure 15. Aircraft can steer without yaw, and there are more options when the terrain is limited or a load is carried.

As shown in Figure 17, the aircraft had a negative pitch angular acceleration and positive roll angular acceleration between 0 and 1 s. The aircraft headed down and rolled to the right, and it flew from the starting point to the right of the front, which was in the negative direction on the X-axis negative and the positive direction on the Y-axis in the inertial reference frame. In Figure 19, the angles of nozzle 1 and nozzle 2 increased, while the angles of nozzle 3 and nozzle 4 decreased between 0 and 1 s. To generate negative pitch angular acceleration, the angles of nozzle 1 and nozzle 2 were increased and the angles of nozzle 3 and nozzle 4 were decreased; to generate positive roll angular acceleration, the angles of nozzle 1 and nozzle 4 were increased and the angles of nozzle 2 and nozzle 3 were decreased. As the aircraft had the two angular accelerations at the same time, the nozzle angles were superimposed, so we found that the angles of nozzle 1 and nozzle 3 changed very much and the angles of nozzle 2 and nozzle 4 changed little. This is consistent with the results of the analysis in Section 5.

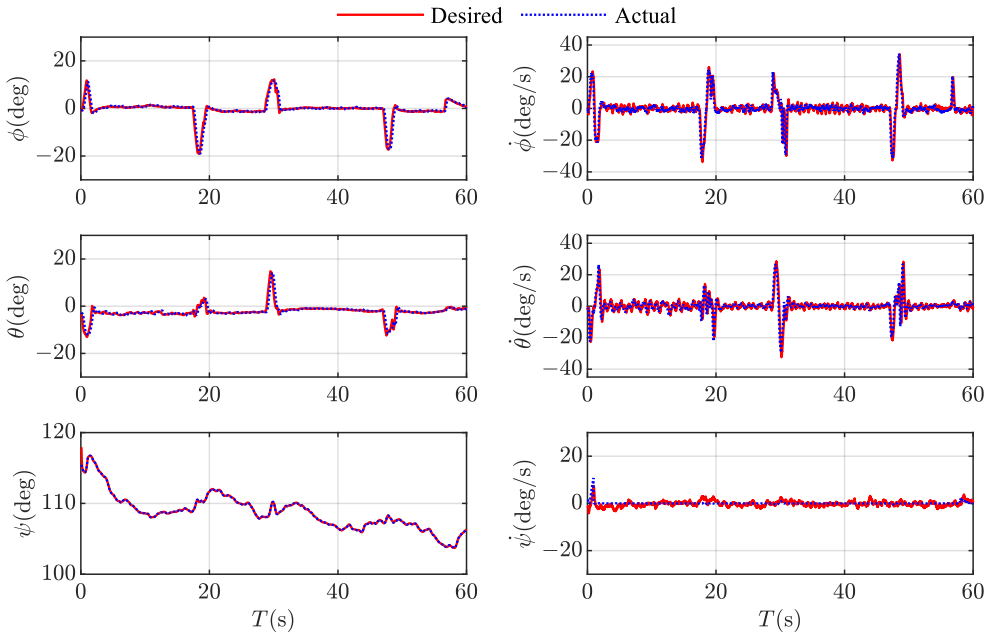

(**a**) (**b**)

Figure 17. Attitude tracking during flight: (**a**) attitude angle tracking response; (**b**) attitude angle velocity tracking response.

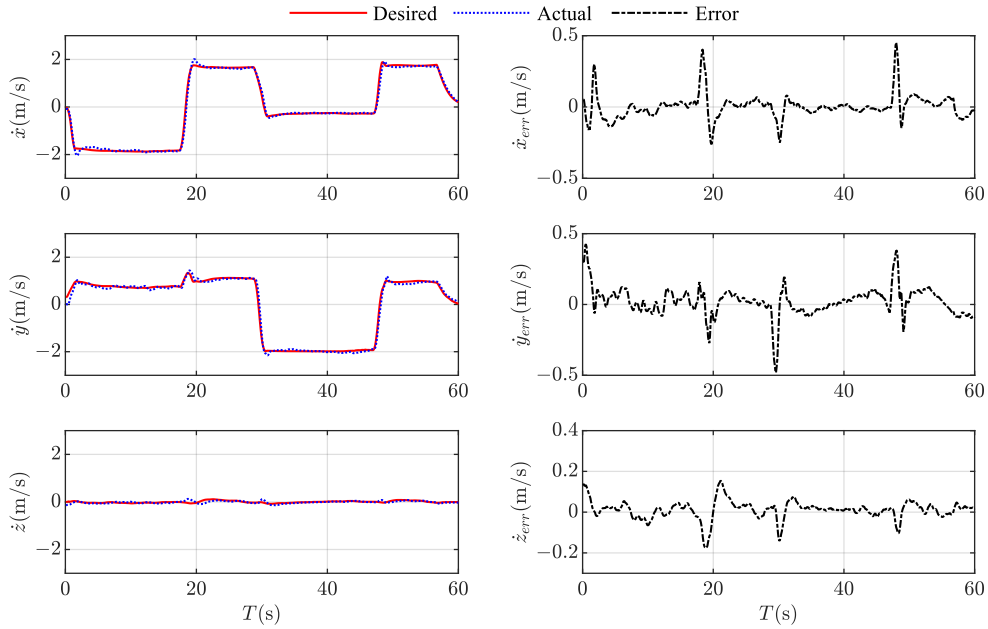

(**a**) (**b**)

Figure 18. Velocity tracking during flight: (**a**) velocity tracking response; (**b**) velocity tracking error.

The one-dimensional thrust vectoring nozzle modules no longer relied on the response speed of the turbojet engine, and the prototype completed the trajectory tracking experiment successfully. The tracking results in three-dimensional space are shown in Figure 20a; there was a position tracking error of approximately 0.2 m, as shown in Figure 20b. Figure 18 shows that there was a maximum velocity overshoot of 15%. There was a phase delay of 0.25 s, as shown in Figure 17. The attitude was stable during flight, and the aircraft followed the desired trajectory well. Trajectory tracking was realized through the experiment and the simulation, which proved that the proposed control schematic is

effective for turbojet aircraft. Compared with the simulation, the error range was larger for the experimental results. First, limitations due to sensor accuracy and measurement and estimation biases were present. Second, the combustion process was uncontrolled, and the thrusts of the four engines were inconsistent. Third, air resistance and gust disturbance occurred during flight. Finally, the center of gravity and inertia of the aircraft changed as fuel was consumed.

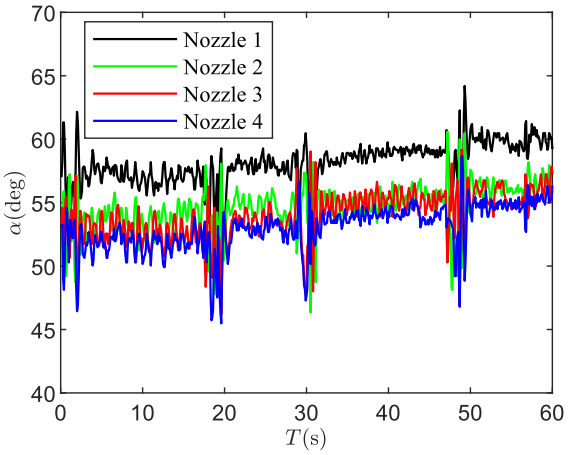

Figure 19. Changes in the angles of the nozzles during flight.

The values of the angle of the nozzle were estimated with the pulse-width modulation (PWM) output of the steering gear because of the presence of the parallel four-bar mechanism. The changes in the angles of the nozzles are shown in Figure 19. As time progressed, the angles of the four nozzles increased gradually as fuel consumption reduced the weight of the aircraft. The angle of nozzle 1 was obviously larger than those of the other nozzles, which was probably because the aircraft was not completely symmetrical, or because there were deviations in the initial installation angles of the steering gear.

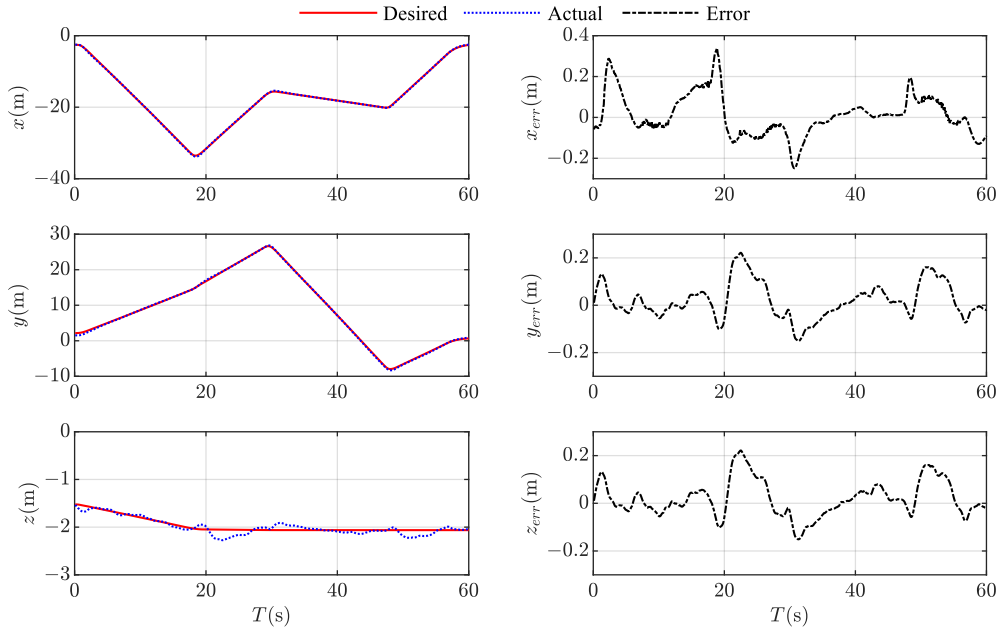

(**a**) (**b**)

Figure 20. Position tracking during flight: (**a**) position tracking response; (**b**) position tracking error.

7. Conclusions

In this study, we demonstrated how an aircraft with one-dimensional thrust vectoring nozzle modules can perform vertical takeoffs and landings. According to the results of simulations and experiments, the one-dimensional thrust vectoring nozzle modules could achieve 87.56% recovery of the turbojet thrust, and the thrust along the engine axis remained unchanged during the rotation of the nozzles. We controlled the position and attitude of the aircraft through the combined movements of the one-dimensional thrust vectoring nozzle modules. The dynamic modeling of the aircraft in the simulations verified the effectiveness of our strategy. We built a prototype for trajectory tracking experiments, and the experimental results showed that the prototype performed well by following the designed control method, which included a good ability to control attitude and position. In addition, the prototype no longer relied on the response speed of the turbojet engine, and it also had the ability to compensate for continuous weight change and uncertain interference.

Throughout the development process, we encountered a series of problems that will form the basis of our future study for developing this platform. Next, we will continue to optimize the aircraft on the basis of this platform to take full advantage of the large thrust-to-weight ratio of the turbojet engine and to improve the load capacity and control accuracy of the aircraft.

Author Contributions: Conceptualization, B.L. and Y.G.; methodology, B.L.; funding acquisition, J.Z. (Jie Zhao); investigation, Y.Z. and Y.G.; methodology, B.L. and L.G.; supervision, X.Z. and J.Z. (Jie Zhao); validation, J.Z. (Junming Zhang); writing—original draft, B.L.; writing—review and editing, Y.G. All authors have read and agreed to the published version of the manuscript.

Funding: This research was funded by the National Natural Science Foundation of China (No. 52205012).

Institutional Review Board Statement: Not applicable.

Informed Consent Statement: Not applicable.

Data Availability Statement: Not applicable.

Conflicts of Interest: The authors declare no conflict of interest.

References

1. Suzuki, S.; Zhijia, R.; Horita, Y.; Nonami, K.; Kimura, G.; Bando, T.; Hirabayashi, D.; Furuya, M.; Yasuda, K. Attitude control of quad rotors QTW-UAV with tilt wing mechanism. *J. Syst. Des. Dyn.* **2010**, *4*, 416–428. [CrossRef]
2. Chen, S. Design of Power Cable UAV Intelligent Patrol System Based on Adaptive Kalman Filter Fuzzy PID Control. In *First International Conference on Real Time Intelligent Systems*; Springer: Berlin/Heidelberg, Germany, 2016; pp. 79–91.
3. Wen, S.; Zhang, Q.; Yin, X.; Lan, Y.; Zhang, J.; Ge, Y. Design of plant protection UAV variable spray system based on neural networks. *Sensors* **2019**, *19*, 1112. [CrossRef] [PubMed]
4. Song, B.D.; Kim, J.; Kim, J.; Park, H.; Morrison, J.R.; Shim, D.H. Persistent UAV service: An improved scheduling formulation and prototypes of system components. *J. Intell. Robot. Syst.* **2014**, *74*, 221–232. [CrossRef]
5. Pounds, P.E.I.; Bersak, D.R.; Dollar, A,M. The yale aerial manipulator: Grasping in flight. In Proceedings of the 2011 IEEE International Conference on Robotics and Automation, Shanghai, China, 9–13 May 2011; pp. 2974–2975.
6. Kim, K.; Spieler, P.; Lupu, E.S.; Ramezani, A; Chung, S.J. A bipedal walking robot that can fly, slackline, and skateboard. *Sci. Robot.* **2021**, *6*, 59–72. [CrossRef] [PubMed]
7. Govindarajan, B.; Sridharan, A. Hybrid Powertrain Systems for Hybrid VTOL Aircraft. In *AIAA AVIATION 2021 FORUM*; American Institute of Aeronautics and Astronautics: Reston, VA, USA, 2021; pp. 3221–3243.
8. Amici, C.; Ceresoli, F.; Pasetti, M.; Saponi, M.; Tiboni, M.; Zanoni, S. Review of propulsion system design strategies for unmanned aerial vehicles. *Appl. Sci.* **2021**, *11*, 5209. [CrossRef]
9. Ko, A.; Ohanian, O.; Gelhausen, P. Ducted fan UAV modeling and simulation in preliminary design. In Proceedings of the AIAA Modeling and Simulation Technologies Conference and Exhibit, Hilton Head, SC, USA, 20–23 August 2007; pp. 6375–6394. [CrossRef]
10. Yan, J.D. Current status and development analysis of lithium-ion batteries. *Acta Aeronaut. Astronaut. Sin* **2014**, *35*, 2767–2775.
11. Armstrong, F.W.; Levine, J. *Overview of the US/UK ASTOVL Program*; SAE Technical Paper; 1987. Available online: https://www.sae.org/publications/technical-papers/content/872365/ (accessed on 15 September 2022).

12. Li, Y.; Li, H.; Wu, L. Li, C. Experimental modeling of micro turbine engine propulsion systems. *J. Tsinghua Univ. (Sci. Technol.)* **2017**, *57*, 107–112.
13. Türkmen, A.; Altuğ, E. Design of a Quad-Jet VTOL UAS for Heavy-lift Applications. In Proceedings of the 2020 International Conference on Unmanned Aircraft Systems (ICUAS), Athens, Greece, 1–4 September 2020; pp. 875–882.
14. Şenkul, F.; Altuğ, E. Modeling and control of a novel tilt-Roll rotor quadrotor UAV. In Proceedings of the 2013 International Conference on Unmanned Aircraft Systems (ICUAS), Atlanta, GA, USA, 28–31 May 2013; pp. 1071–1076.
15. Traskos, R.; Schweinfurth, R.; Anders, G. USN/FMOD FRG VAK-191B joint flight test program. In *Aircraft Description and Flight Test*; 1976. Available online: https://apps.dtic.mil/sti/citations/ADA040535 (accessed on 10 September 2022).
16. Cen, Z.; Smith, T.; Stewart, P.; Stewart, J. Integrated flight/thrust vectoring control for jet-powered unmanned aerial vehicles with ACHEON propulsion. *Proc. Inst. Mech. Eng. Part G J. Aerosp. Eng.* **2015**, *229*, 1057–1075.
17. Wu, L.; Li, H.; Li, Y.; Li, C. Position tracking control of tailsitter VTOL UAV with bounded thrust-vectoring propulsion system. *IEEE Access* **2019**, *7*, 137054–137064. [CrossRef]
18. Muehlebach, M.; D'Andrea, R. The flying platform—A testbed for ducted fan actuation and control design. *Mechatronics* **2017**, *42*, 52–68. [CrossRef]
19. Ale Isaac, M.S.; Luna, M.A.; Ragab, A.R.; Ale Eshagh Khoeini, M.M.; Kalra, R.; Campoy, P.; Flores Peña, P.; Molina, M. Medium-Scale UAVs: A Practical Control System Considering Aerodynamics Analysis. *Drones* **2022**, *9*, 244. [CrossRef]
20. Gustafson, R.A. Ten years of US marine corps harrier operations. In *AGARD The Impact of Mil. Appl. on Rotorcraft and V/STOL Aircraft Design p 10(SEE N 81-33137 24-01)*; 1981. [CrossRef]
21. Hess, J.R.; Bear, R.L. Study of aerodynamic technology for single-cruise-engine V/STOL fighter/attack aircraft. In *DC: National Aeronautics and Space Administration (NASA)*; 1987. Available online: https://ntrs.nasa.gov/citations/19840020668 (accessed on 30 August 2022). [CrossRef]
22. Liu, S,Y. The Design and Performance Study of the Icing Wind Tunnel Corner and Corner Vane. Master's Thesis, Nanjing University of Aeronautics and Astronautics, Nanjing, China, 2011.
23. Gelder, T.; Moore, R.; Sanz, J.; Mcfarland, E. Wind tunnel turning vanes of modern design. In Proceedings of the 24th Aerospace Sciences Meeting, Reno, NV, USA, 6–9 January 1986; pp. 44–58.
24. Menter, F.R. Two-equation eddy-viscosity turbulence models for engineering applications. *AIAA J.* **1994**, *32*, 1598–1605.
25. Mihaescu, M.; Semlitsch, B.; Fuchs, L.; Gutmark, E. Assessment of turbulence models for predicting coaxial jets relevant to turbofan engines. In Proceedings of the Conference on Modelling Fluid Flow (CMFF 12), The 15th International Conference on Fluid Flow Technologies, Budapest, Hungary, 4–7 September 2012; pp. 4–7.
26. Zhao, J.; Ding, X.; Jiang, B.; Jiang, G.; Xie, F. A novel control strategy for quadrotors with variable mass and external disturbance. *Int. J. Robust Nonlinear Control* **2021**, *31*, 8605–8631. [CrossRef]